The hit position reconstruction algorithm for neutron and gamma imaging detectors based on artificial neural networks

Penghui Wang[1], Yiyang Long[1], Jifeng Han[1, *], Yangmei Chen[1], Peng Hu[4], Chuang Liu[3], Weiping Lin[1], Xingquan Liu[1], Guofeng Qu[1], Sen Qian[2], Jing Ren[3], Peipei Ren[1], Ruiqiang Song[1], Ke Wang[2], Chuqi Yi[1], Shenghua Yin[4], Chaoyang Zhao[1]

[1]Key Laboratory of Radiation Physics and Technology of the Ministry of Education, Institute of Nuclear Science and Technology, Sichuan University, Chengdu 610064, China

[2]Institute of High Energy Physics, Chinese Academy of Sciences, Beijing 100049, China

[3]Key Laboratory of In-fiber Integrated Optics of Ministry of Education, College of Physics and Optoelectronic Engineering, Harbin Engineering University, Harbin 150001, China

[4]China Nuclear (Beijing) Nuclear Instrument CO., LTD, Beijing 100176, China

*Corresponding author. E-mail address: hanjf@scu.edu.cn

Abstract:

Neutron and gamma imaging have continuously expanded applications in nuclear safety, national security, and materials characterization. The hit position reconstruction algorithm is a key issue that constrains the image fidelity and accuracy. This work has developed a two-dimensional planar neutron and gamma imaging system based on a monolithic lithium glass scintillator and a silicon photomultiplier array. The results from the three metrics position nonlinearity response, flood image uniformity, and useful field-of-view demonstrate that the proposed artificial neural network (ANN) method significantly advances over traditional reconstruction methods. Imaging results from both the '720' and 'SCU' models confirm the ANN method's superior reconstruction quality. In addition, the ANN method achieves a systematic neutron imaging spatial resolution of approximately 0.47 mm for the 'T' model. These algorithms are implemented in experimental imaging system, the ANN method maintains acceptable image quality although certain noise artifacts are found, confirming its applicability in both simulated and experimental settings. This work demonstrates that the ANN method significantly enhances positioning accuracy and computational efficiency, resulting in superior neutron/gamma imaging quality.

Keywords: Lithium glass; Neutron imaging; Position reconstruction; Artificial neural network; Spatial resolution

1.Introduction

Nuclear energy, recognized as a clean, low-carbon, and efficient source for baseload power generation, has been developed and utilized by major nuclear power nations worldwide[1]. Radiographic imaging is a widely used modern technology in nuclear energy applications, which involves projecting a radiation beam through an object onto a detector, and the object's internal structure can be reconstructed through a computer-based data acquisition and analysis system[2]. This technique has broad applications in fields such as medicine[3, 4], security screening[5, 6], and cultural heritage research[7, 8]. Particularly, from the 1995 sarin gas attacks on the Tokyo subway system[9] to the catastrophic 9/11 attacks in 2001[10], and more recently, the

2017 Manchester Arena bombing[11], transnational terrorist incidents have consistently demonstrated their capacity to undermine global security infrastructures. These high-profile attacks, spanning nearly three decades and affecting diverse regions, highlight the persistent evolution of threats to civilian protection mechanisms worldwide. Therefore, the importance of reliable radiographic imaging technology for non-destructive detection systems that identify hazardous materials and inspect the interior of objects is self-evident to the international community.

Radiographic imaging constitutes a critical methodology within non-destructive testing, encompassing three principal modalities: X-ray, gamma-ray, and neutron imaging[12]. X-ray and gamma imaging technologies have achieved significant technological maturity, demonstrating robust reliability in industrial and security applications. In contrast, neutron imaging remains an emerging field with specialized use cases. Hal Anger invented the first gamma camera in 1957 [13], and it is still widely used today. Although the performance of gamma cameras continues to improve, and various gamma imaging systems have been developed, the design of most of these systems is fundamentally based on the Anger camera. A novel gamma imaging system was proposed, utilizing forward-scattered Compton recoil electrons to achieve indirect energy-selective gamma imaging[14]. Machine learning algorithms based on Gradient Boosted Decision Trees and Deep Neural Networks were developed to study the effects of source position reconstruction in gamma coded aperture imaging systems[15]. An image resolution of about 90 μm was successfully achieved by introducing a virtual source method to optimize bremsstrahlung radiography, even after gamma-ray passed through a 100 mm steel object[16].

Neutron imaging technology shares many similarities with gamma imaging in principle. However, neutron beams, particularly thermal neutrons, exhibit strong penetrating capabilities for heavy metal elements, yet they are susceptible to light materials and different isotopic compositions within substances[17]. This sensitivity makes neutron imaging technology an important complementary to gamma imaging. In specialized fields such as the detection of internal defects in nuclear fuel elements[18], core loss inspection of aircraft engine blades[19], distribution of lithium-ion in batteries, and water management in fuel cells[20-22], neutron imaging demonstrates superior performance compared to gamma imaging.

The hardware and the position reconstruction algorithms primarily influence the quality of reconstructed images in gamma and neutron imaging. Improving the position reconstruction algorithm has addressed some issues caused by hardware limitations, significantly enhancing the overall system performance of gamma and neutron imaging[23-26]. Moreover, upgrading the position reconstruction algorithm to improve image quality is often more feasible and cost-effective than upgrading the hardware. Early reconstruction algorithms primarily relied on the classical Center-Of-Gravity (COG)[13], which has advantages such as simple principles, ease of development, and high computational efficiency. However, it suffers from issues like image edge compression and distortion effects[23, 26]. In recent years, many proposed improvements to position reconstruction algorithms have been based on the classical COG, such as the Truncated Center-Of-Gravity (TCOG)[27]. Setting a

threshold helps reduce the impact of noise and small signals from distant event areas, significantly aiding in noise elimination and expanding the useful Field-Of-View. Another method, the Raise-To-Power (RTP)[25], involves applying a power function to the collected signals to increase the weight of more significant signals, thereby enhancing spatial resolution. Additionally, the least squares estimator method has been increasingly used in recent years to calculate the position of scintillation events associated with a given charge distribution. The main principle involves constructing a cost function based on the sum of squared residuals between the measured electrical signals and the fluorescence distribution model, transforming it into a least squares estimation problem for position estimation. Particle swarm optimization is then employed to solve the least squares problem, resulting in the Least Squares Estimator based on Particle Swarm Optimization (PSO-LSE)[26]. This approach improves imaging performance parameters such as spatial resolution and useful Field-Of-View. However, it requires considerable computational time. Similar reconstruction algorithms include look-up table estimation[28], maximum likelihood (ML)[29], and others. Many studies have been carried out to explore the effects of these reconstruction algorithms on the performance of neutron and gamma imaging. The gamma experimental data were evaluated using various traditional reconstruction algorithms, and the PSO-LSE algorithm achieved the best performance in terms of the peak-to-valley ratio, useful Field-Of-View, and position linearity response[30]. Data obtained from the Cerium doped Lutetium-based crystal array and SiPM array were used, and multiple-class neural network and binary classification neural network algorithms were applied to predict the position of scintillation events of gamma-ray, achieving an average accuracy of 85%, which surpassed the COG method[31]. A neutron camera based on a ^{6}Li scintillator glass and SiPM array was built, and a spatial resolution with a full width at half maximum better than 0.6 mm was achieved using a statistical iterative ML algorithm[32].

All position reconstruction algorithms mentioned above have limitations to some extent. Artificial neural network (ANN) has been proven to be very effective in solving complicated problems. Therefore, this work proposes a position reconstruction algorithm based on ANN. The performance of these reconstruction algorithms has been evaluated by metrics of the position nonlinearity response, flood image uniformity, useful Field-Of-View, Contrast-To-Noise Ratio, Information Entropy, Gradient Magnitude, and spatial resolution. Finally, the feasibility of the proposed algorithm is further validated through experimental data.

2. Monte-Carlo simulation and experimental design
2.1 Geant4 simulation

The simulation of neutron and gamma imaging systems is based on the Geant4.10.07 package[33, 34]. The simulation result is subsequently processed to compare the effectiveness of various position reconstruction algorithms. The imaging model of the two-dimensional planar detector is shown in Fig. 1, including a monolithic ^{6}Li scintillator glass (GS20)[35, 36], an Enhanced Specular Reflector (ESR) reflective layer, an 8 * 8 silicon photomultiplier (SiPM) array, and a monolithic

printed circuit board (PCB). The thickness of the GS20 is 3 mm, and ^{6}Li is enriched to 95% to realize high neutron detection efficiency. The surfaces of the GS20 are covered with ESR, except the light-output surface. The SiPM array, which is positioned within the PCB, is directly coupled to the back of the GS20. The effective photosensitive area is 3 * 3 mm² for each SiPM pixel, and a 0.2 mm gap is set to separate these SiPM pixels. Within the Geant4 simulation framework, the GLISUR model is employed to characterize the optical surface. An air layer is configured between the GS20 and ESR layers, while the dielectric-dielectric surface type is specified for the boundary between air and GS20. Similarly, the dielectric-metal surface type is used for the boundaries between ESR and air. Additionally, for the ESR boundary, the photon-electric efficiency is set to 0 and the reflectivity to 0.985, while for the GS20 boundary, the surface polishing and reflectivity are set to 1.

The total training dataset is obtained from the Geant4 simulation described above. Specifically, neutron or gamma is injected at intervals of 0.5 mm within the detector's imaging area. Then, the two-dimensional 8 * 8 photon information collected by the SiPM array for each event is recorded into the ANN model. For each injected position, 2000 events are simulated, and 5,202,000 events are acquired to test the reconstruction algorithm.
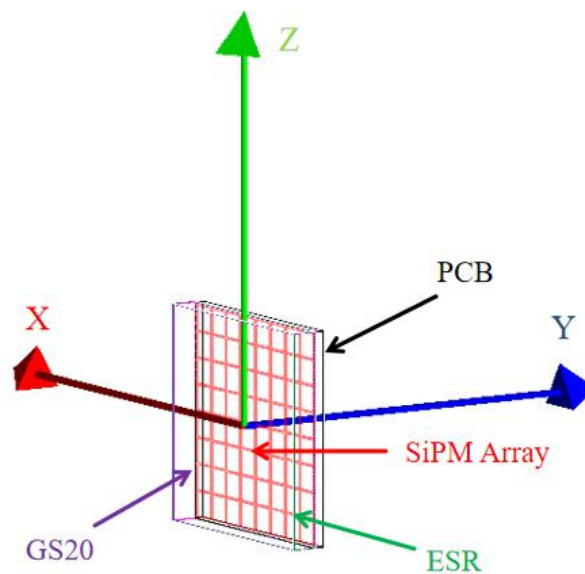

Fig. 1 Schematic diagram of the two-dimensional planar detector imaging system

When thermal neutron hits the GS20, it can be detected through the capture reaction of ^{6}Li (n, t) ^{4}He with the Q value of 4.78 MeV.

The energy of the secondary particles would be deposited in the GS20, and scintillating photons could be generated through the Ce^{3+} activator. This activator offers high light yield and fast response due to its dipole 5d - 4f transition. This

scintillating effect is practical for gamma-ray, except that the energy is deposited by secondary electrons generated through the photoelectric effect or Compton scattering. Finally, the optical photons are detected and transferred to electrical signals by the SiPM array. Based on the light distribution detected by the SiPM array, the hit position of the injected neutron or gamma particle is calculated using different algorithms.

2.2 Experimental design

A physical prototype of the two-dimensional planar detector imaging system has been built, as shown in Fig. 2. The detector consists of a GS20 with a density of 2.3 g/cm^3 and a light yield of 2000 photons/MeV, a SiPM array (HAMAMATSU S14161-3050HS-08) with a 50 μm pixel pitch, and ESR (3M), along with a 64-channel Application Specific Integrated Circuit (ASIC) acquisition card (CAEN A5202), which transmits the data collected to a computer for image reconstruction.
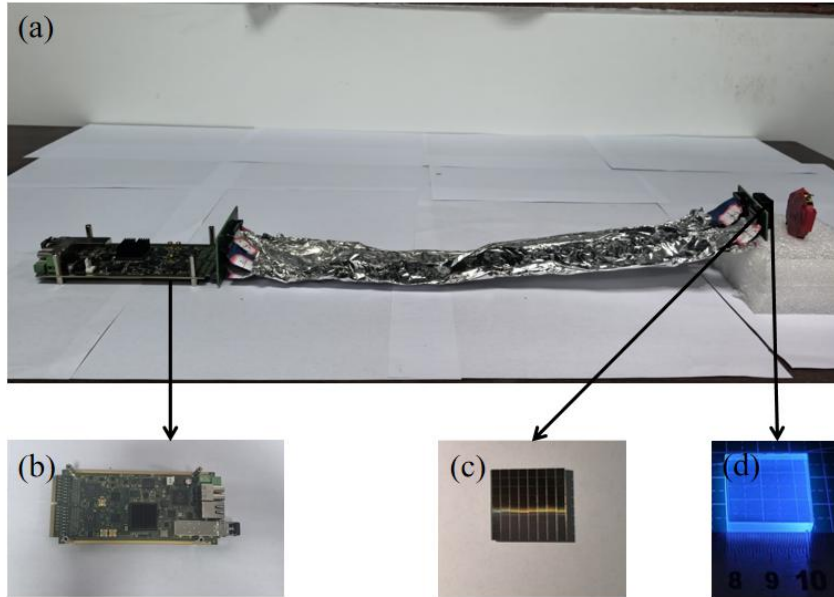

Fig. 2 Schematic diagram of the two-dimensional detector imaging structure: (a) Overall structure; (b) 64-channel ASIC acquisition card; (c) SiPM array; (d) GS20 (Under ultraviolet illumination)

3. Reconstruction algorithms

When the rays are injected into the GS20 at position $P(x_0, y_0)$, the optical photons generated would be distributed to various SiPMs. For the SiPM located at $n(i,j)$, where i,j are within $[1, N]$, the SiPM's position is represented by its center $C(x_{ij}, y_{ij})$, and q_{ij} is the electrical signal value collected by this SiPM.

3.1 COG method

The COG, also known as the Anger algorithm, remains a fundamental technique and basic principle for position reconstruction in scintillation cameras. For the N * N

SiPM array, the hit position can be obtained from equation (1):

$$x_0 = \frac{\sum_{i,j=1}^{N} q_{ij} \cdot x_{ij}}{\sum_{i,j=1}^{N} q_{ij}}, y_0$$

$$= \frac{\sum_{i,j=1}^{N} q_{ij} \cdot y_{ij}}{\sum_{i,j=1}^{N} q_{ij}} \quad (1)$$

3.2 TCOG method

The TCOG, as an improved version of COG, improves imaging resolution by setting a threshold (θ) to remove interference factors such as small signals far away from the event location and random noise. In this work, the threshold for each event was set to 5% of the maximum signal value in each event. In the TCOG algorithm, the hit position can be obtained from equations (2) and (3):

$$x_0 = \frac{\sum_{i,j=1}^{N} F(q_{ij}) \cdot x_{ij}}{\sum_{i,j=1}^{N} F(q_{ij})}, y_0$$

$$= \frac{\sum_{i,j=1}^{N} F(q_{ij}) \cdot y_{ij}}{\sum_{i,j=1}^{N} F(q_{ij})} \quad (2)$$

$$F(q_{ij}) = \begin{cases} q_{ij}, & q_{ij} \geq \theta \\ 0, & q_{ij} < \theta \end{cases} \quad (3)$$

3.3 RTP method

The RTP, another modification of the classical Anger algorithm based on the power operation, can effectively improve the spatial resolution of crystal cameras, reduce compression effects and distortion of positioning results, and calculate the interaction position of ray with scintillation crystal by weighted power calculation of the center of mass of charge distribution. In the RTP algorithm, the hit position can be obtained from equation (4):

$$x_0 = \frac{\sum_{i,j=1}^{N} F(q_{ij})^{\alpha} \cdot x_{ij}}{\sum_{i,j=1}^{N} F(q_{ij})^{\alpha}}, y_0$$

$$= \frac{\sum_{i,j=1}^{N} F(q_{ij})^{\alpha} \cdot y_{ij}}{\sum_{i,j=1}^{N} F(q_{ij})^{\alpha}} \quad (4)$$

where α is a weight coefficient greater than 1, and α is set to 1.3 in this work after optimization.

3.4 PSO-LSE method

The PSO-LSE iteratively calculates the position of the scintillation event corresponding to a given charge distribution through optimization[26]. The theoretical framework of the PSO-LSE algorithm consists of two components: an objective

function defined by the sum of squared residuals between the detected charge signals and the model function representing the light distribution of the scintillation event, and the PSO method, which is used to find the optimal solution to the objective function. The objective function established based on the signals collected by the SiPM is shown in equation (5):

$$F_{obj}(x_0, y_0) = \sum_{i,j=1}^{N}\left[I(x_{ij}, y_{ij}) - q_{ij}\right]^2 \quad (5)$$

Thus, the estimation of the scintillation event position becomes to find the minimum value of equation (5), which is a least squares problem as described in equation (6):

$$min\left\{\sum_{i,j=1}^{N}\left[I(x_{ij}, y_{ij}) - q_{ij}\right]^2\right\} \quad (6)$$

In equations 5 and 6, $I(x_{ij}, y_{ij})$ is the theoretical light intensity of SiPM $n(i,j)$ when the supposed scintillation event position is at $P(x_0, y_0)$. Generally, in continuous crystals, the spatial density distribution of scintillation fluorescence is commonly described with the Scrimger-Backer model[37]:

$$I(x_{ij}, y_{ij}) = \frac{I_0}{\left[1 + \frac{(x_{ij} - x_0)^2 + (y_{ij} - y_0)^2}{t^2}\right]^{3/2}} \quad (7)$$

where I_0 is the light distribution amplitude, t is the distance between the SiPM $n(i, j)$ and supposed hit position $P(x_0, y_0)$.

The least squares method determines the parameters (I_0, t, x_0, y_0) that best fit the Scrimger–Backer model to the signal distribution of the SiPM array. Therefore, the problem of solving the fitted parameters becomes the optimization of minimizing the objective function (5). PSO, as an optimization algorithm, proves to be highly advantageous for solving the optimization of minimizing the objective function[26]. To address the slow convergence speed and convergence issues of the standard PSO, this paper employs a method that dynamically adjusts the step size factor based on the average evaluation value and initializes particles using a uniform distribution. First, the PSO algorithm requires randomly generating a set of initial solutions to initialize the particle swarm. In this paper, the initial solutions are generated by uniformly distributing the initial coordinates (x_0, y_0) of several particles within the coordinate range of the SiPM array. The initial velocity of each particle is set, and the initial amplitude value I0 of the light distribution is randomly assigned between the minimum and maximum values of the signals collected by the SiPM array. The initial distance t between the ray's hit position with the crystal and the SiPM array is set from 0 to 3.

Additionally, the PSO algorithm tends to iterate toward the best-known positions, which can result in incomplete coverage of the search space during the algorithm's

execution. This increases the likelihood of overlooking important information. Some particles may lose activity due to reduced velocity, causing the optimization process to terminate prematurely and the algorithm to become trapped in a local optimum. Therefore, the algorithm's ability to escape local optima is enhanced by utilizing the average evaluation value of all particles in a specific dimension to control the step size factor.

3.5 ANN method

In recent years, ANN has experienced rapid development and has found applications in nuclear technology fields, such as neutron/gamma discrimination[38, 39] and explosive material prediction[40].

The fully connected neural network (FCNN)[41] and residual neural network (ResNet)[42] models are constructed using Google's Keras and TensorFlow packages. The structural diagrams of the two ANN models are shown in Fig. 3. The input of these ANN models is the signal distribution of the SiPM array, while the output is the predicted two-dimensional hit position. The FCNN architecture consists of four fully connected layers, each followed by a ReLU activation function, with a final linear layer used for coordinate prediction, as illustrated in Fig. 3(a). The FCNN provides a baseline model for understanding the problem. The ResNet architecture includes a spatial feature extraction module consisting of two consecutive 7 * 7 convolutional layers. Each convolutional layer is followed by batch normalization, ReLU activation, and dropout for regularization. This spatial feature extraction module is repeated nine times within the ResNet architecture. In addition, to mitigate the vanishing gradient problem and enhance the model's performance, The ResNet architecture also incorporates skip connections into each module, as illustrated in Fig. 3(b). Each skip connection includes a 7 * 7 convolutional layer applied within each spatial feature extraction module.
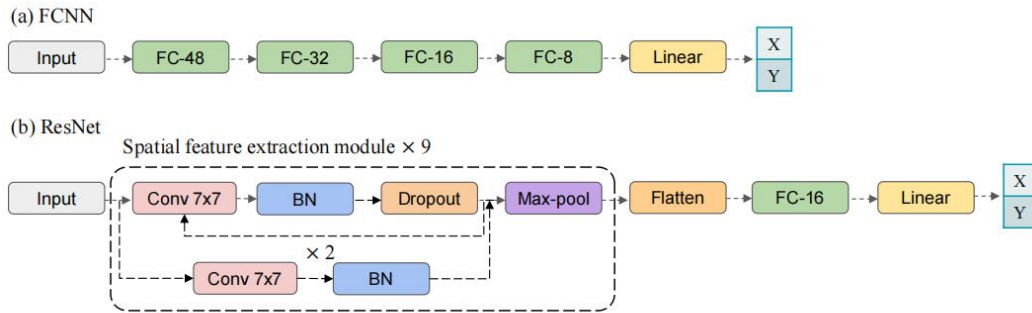

Fig. 3 Neural network structures: (a) FCNN; (b) ResNet

80% of the dataset is randomly chosen for model training, the remaining 20% is used for testing, and 20% of the trainset is used for validation during training. After 50 epochs, the prediction accuracies of the ANN model for neutron and gamma are shown in Fig. 4 and Fig. 5, respectively. The accuracy is better than 96.5% for all models.
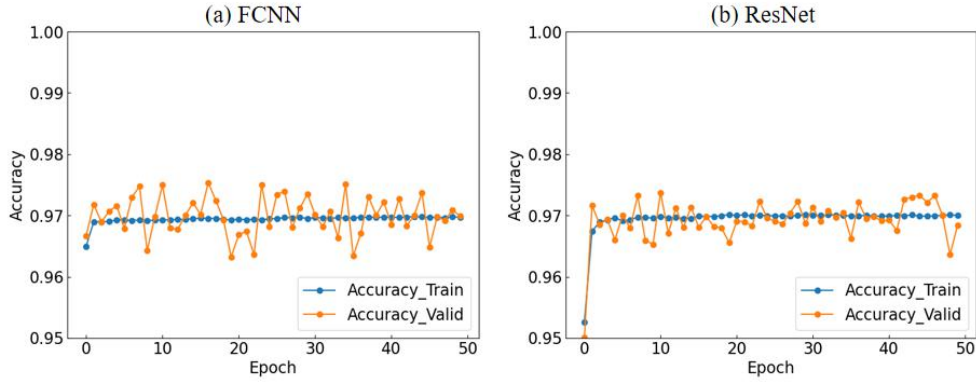
Fig. 4 Neutron model accuracy during training: (a) FCNN; (b) ResNet
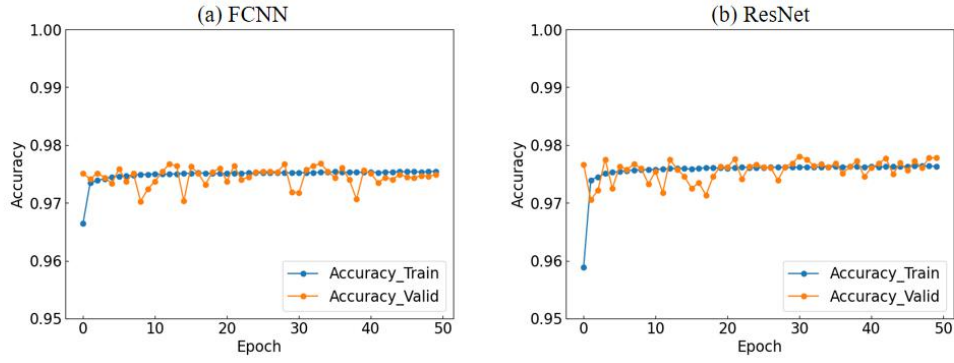

Fig. 5 Gamma model accuracy during training: (a) FCNN; (b) ResNet

4. Reconstruction performance evaluation

4.1 Neutron imaging

4.1.1 Position nonlinearity response (PNR) for neutron

The PNR is one of the most important indicators of imaging quality, where the reconstructed positions are compared with the injected actual positions, and the functional relationship between them is acquired. To better evaluate the neutron PNR, a scatter plot of the actual positions versus the residuals of the reconstructed neutron positions for different algorithms is calculated, as shown in Fig. 6. In this work, the mean squared errors (MSE) of the residuals of the reconstructed positions for different algorithms are calculated, as shown in Table 1.
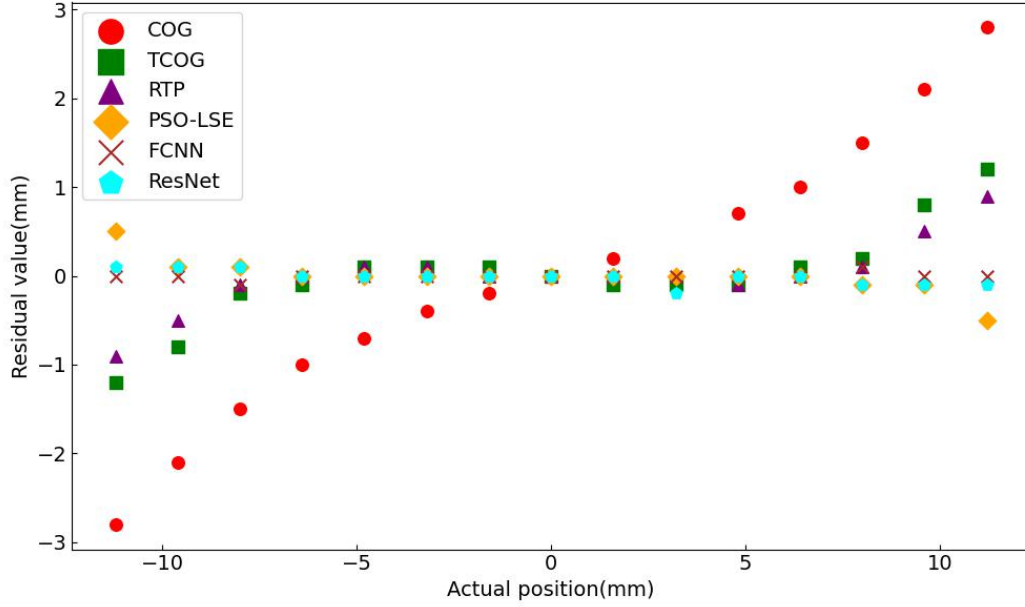
Fig. 6 Residual plot of reconstructed positions for different algorithms

Table 1 MSE values of various reconstruction algorithms

	COG	TCOG	RTP	PSO-LSE	FCNN	ResNet
MSE	2.149	0.288	0.145	0.036	**0.001**	0.007

Based on the MSE values for neutron imaging, the PSO-LSE and ANN methods exhibit better PNR performance, resulting in higher position reconstruction accuracy and more minor errors. All algorithms can reconstruct the positions accurately for the central region, while the ANN method exhibits better accuracy in reconstructing positions at the edge region.

4.2.2 Flood image uniformity and useful Field-Of-View (UFOV) for neutron imaging

Flood image uniformity is an important indicator that reflects the inherent performance of the imaging system. Here, it refers to placing the detector in a uniform radiation field generated by an uncollimated neutron point source and then reconstructing the image after a specific measurement period. The neutron flood image results for different reconstruction algorithms are shown in Fig. 7. To evaluate the effectiveness of these algorithms at the edges of the GS20, the UFOV values are obtained from the flood image, as shown in Table 2. Additionally, to assess the uniformity of the flood image, the relative standard deviations (RSD) for different reconstruction algorithms are calculated and presented in the same table. The UFOV values reflect edge performance, while the RSD values indicate image uniformity.
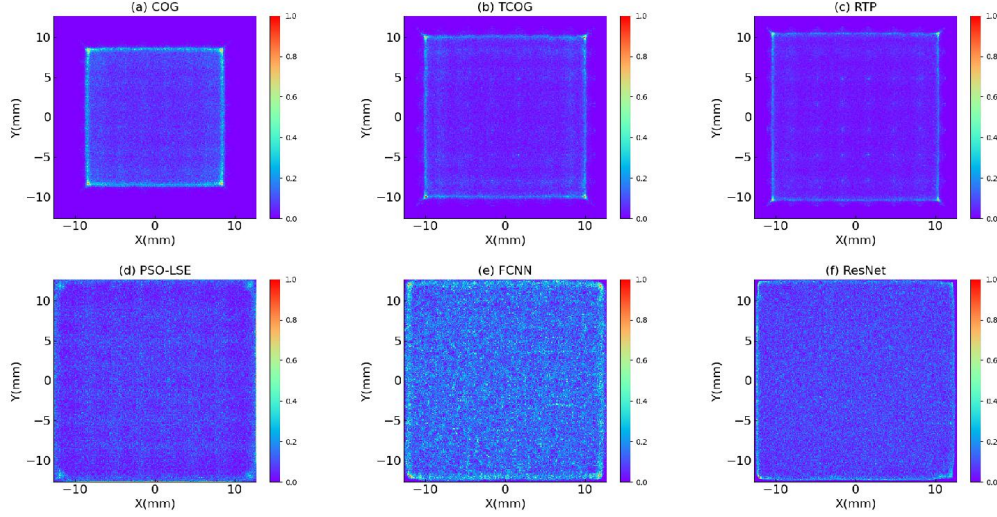
Fig. 7 Results of neutron flood image with different reconstruction algorithms: (a) COG; (b) TCOG; (c) RTP; (d) PSO-LSE; (e) FCNN; (f) ResNet

Table 2 UFOV and RSD values of neutron flood image obtained by various reconstruction algorithms

	COG	TCOG	RTP	PSO-LSE	FCNN	ResNet
UFOV	67.0%	80.3%	82.7%	**98.4%**	96.9%	97.6%
RSD	1.381	1.091	1.118	0.825	**0.619**	0.645

Based on the results, the traditional COG exhibits a compression effect at the edges, significantly reducing the UFOV. The TCOG and RTP methods can expand the imaging range, but its performance is not ideal. On the other hand, the PSO-LSE and ANN methods can improve UFOV to higher than 96%, effectively overcoming the edge suppression issue of COG. Additionally, COG, TCOG, and RTP exhibit RSD values greater than 1 due to their higher edge counts in flood images, resulting in poorer uniformity in the reconstructed images. In contrast, the PSO-LSE and ANN methods demonstrate RSD values below 1, indicating superior uniformity in their reconstructed images.

4.1.3 Neutron model imaging

To further validate the imaging performance of these algorithms, two letter models of '720' and 'SCU' are used for neutron imaging by simulation. The material of the models is cadmium, and the thickness is 4 mm, as shown in Figs. 8a and 8b. In addition, the 'T' model shown in Fig. 8c is also used to calculate the spatial resolution of neutron/gamma imaging, and detailed descriptions can be found in Sections 4.1.4 and 4.2. The neutron imaging of the '720' and 'SCU' models under different reconstruction algorithms are shown in Figs. 9 and 10. To objectively evaluate the imaging quality of different reconstruction algorithms, three metrics, Contrast-To-Noise Ratio (CNR)[43-45], Information Entropy (IE)[46], and Gradient Magnitude (GM)[47], are used to assess the reconstructed images. CNR generally characterizes the contrast between a region of interest (ROI) and background noise in

an image. The area of 'SCU' or '720' in the image is chosen as the ROI range, as exemplified by the black-line enclosed regions in Figs. 9e and 10e, while the other area is chosen as background. A higher CNR value indicates better quality of the reconstructed image. IE and GM are employed to characterize the overall quality of the entire image. The higher the quality, the more information and gradients the image contains, leading to more significant values for IE and GM. To conclude, larger CNR, IE, and GM indicate better performance. The evaluation results are shown in Table 3.
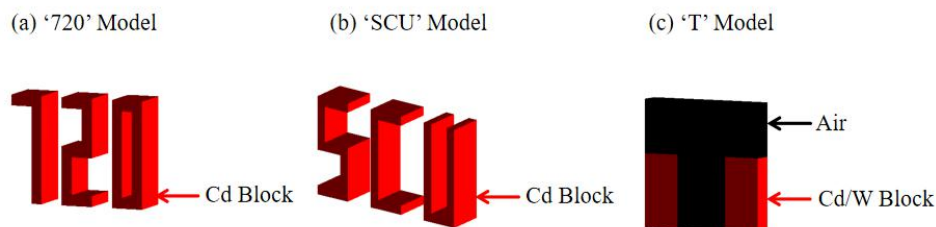

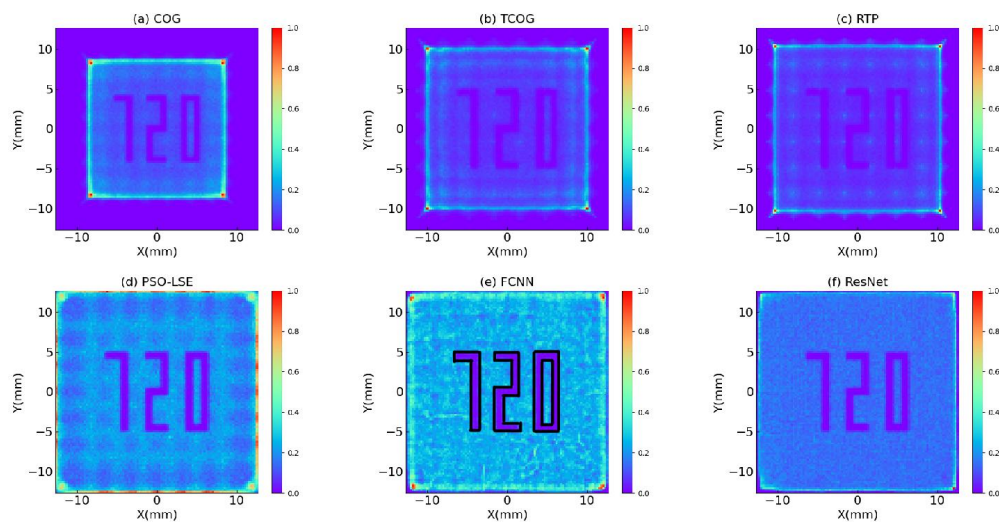**Fig. 8** Neutron/gamma imaging models: (a) '720'; (b) 'SCU'; (c) 'T'

Fig. 9 Imaging results of the '720' model using different reconstruction algorithms: (a) COG; (b) TCOG; (c) RTP; (d) PSO-LSE; (e) FCNN; (f) ResNet
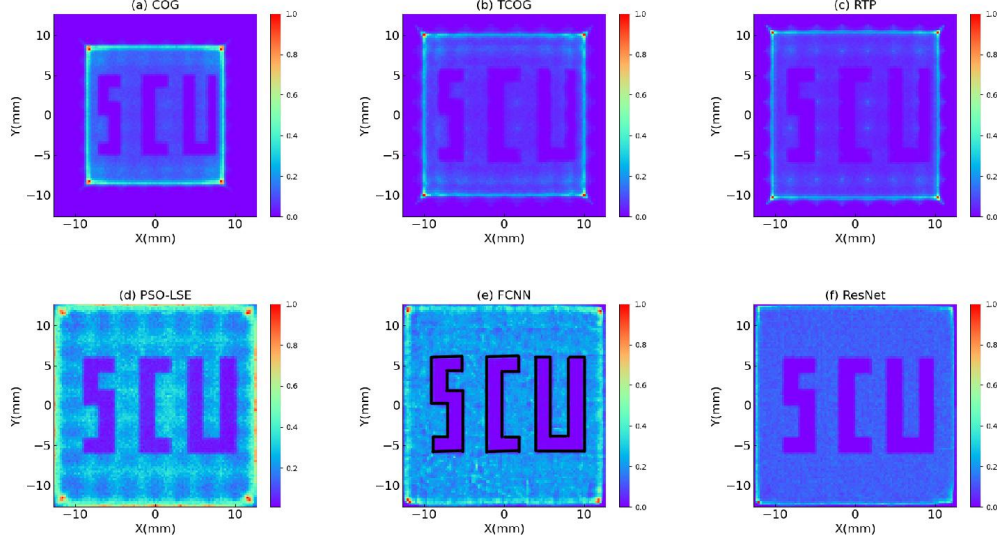
Fig. 10 Imaging results of the 'SCU' model using different reconstruction algorithms:
(a) COG; (b) TCOG; (c) RTP; (d) PSO-LSE; (e) FCNN; (f) ResNet

Table 3 Quality evaluation table for the reconstructed images of the Cd models using
different reconstruction algorithms

Model		COG	TCOG	RTP	PSO-LSE	FCNN	ResNet
	CNR	228.55	**237.14**	232.78	203.54	228.09	225.00
'720'	IE	4.20	4.95	4.71	6.04	**6.14**	5.18
	GM	0.16	0.15	0.14	0.26	**0.31**	0.16
	CNR	226.93	233.23	**233.41**	220.37	228.44	226.09
'SCU'	IE	3.90	4.66	4.44	**6.58**	6.02	4.95
	GM	0.16	0.14	0.14	**0.28**	**0.28**	0.15

Based on the results presented in Table 3, it is observed that for both the '720' model and 'SCU' model, the maximum CNR values are achieved by TCOG and RTP reconstruction methods, respectively. However, these methods yield lower IE and GM values, indicating that the reconstructed images contain less effective information and gradient details. Moreover, the most significant limitation remains the insufficient mitigation of image edge suppression artifacts. In contrast, the proposed FCNN method in this study demonstrates superior performance across all three-evaluation metrics (CNR, IE, and GM) while effectively reconstructing the entire imaging region with enhanced fidelity. These comprehensive results demonstrate that the proposed ANN method, particularly the FCNN method, delivers superior overall image reconstruction quality.

Noises are available in the reconstructed image, and filtering methods are often applied for denoising. Fig. 11 shows the images after applying mean filtering[48] and median filtering [49] for the FCNN results. The quantitative evaluation results of the filtering images processed by the FCNN method are presented in Table 4.
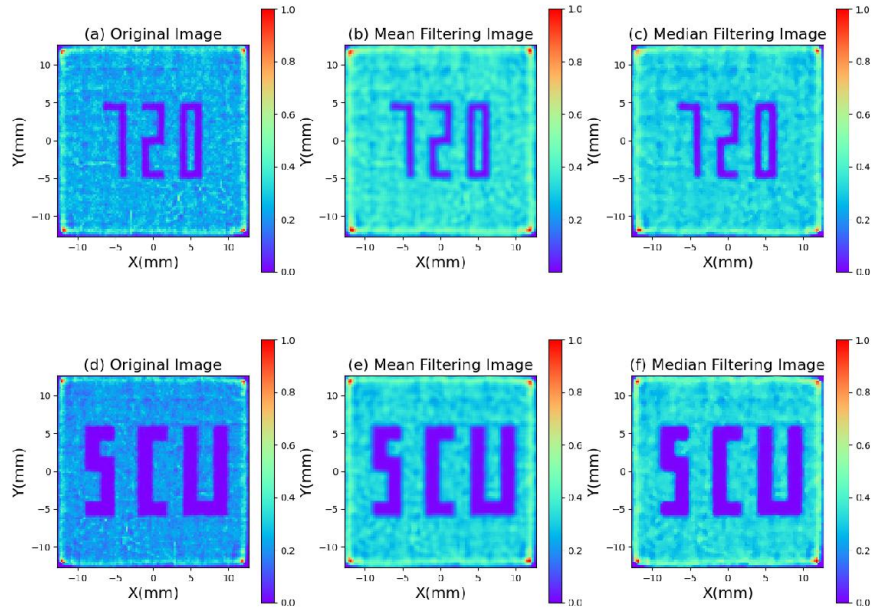
Fig. 11 Image after applying denoising algorithms to the FCNN reconstruction results: (a) Original image of the '720' model; (b) Mean Filtering image of the '720' model; (c) Median Filtering image of the '720' model; (d) Original image of the 'SCU' model; (e) Mean Filtering image of the 'SCU' model; (f) Median Filtering image of the 'SCU' model

Table 4 Quality evaluation table for the reconstructed images of the Cd models using FCNN method (After filtering algorithm)

Model		Original image	Mean filtering image	Median filtering image
	CNR	228.09	**243.00**	235.82
'720'	IE	**6.14**	5.53	5.40
	GM	**0.31**	0.12	0.16
	CNR	228.44	**243.03**	236.06
'SCU'	IE	**6.02**	5.76	5.42
	GM	**0.28**	0.13	0.15

Based on the results presented in Table 4, the mean filtering method achieves the highest CNR value, demonstrating its effectiveness in noise reduction to a certain extent. However, this filtering approach simultaneously compromises the information content and gradient variations within the image, reducing IE and GM values in the reconstructed images.

4.1.4 Spatial resolution (SR)

The SR of an imaging system is one of the key indicators for evaluating its imaging capability. It refers to the system's ability to distinguish between two adjacent objects. The better the SR, the stronger the system can discern subtle object

differences. A criterion is needed to evaluate an imaging system's SR. The Modulation Transfer Function (MTF) is one widely used method for representing SR. This standard allows for a precise, convenient, and straightforward comparison of resolution through numerical or graphical representations[50].

A commonly used practical method to obtain the system's MTF is through the image of opaque objects with sharp edges, known as the knife-edge method. In this study, the 'T' model shown in Fig. 8c is employed to calculate the system's SR using the knife-edge method, primarily consisting of the following three steps. First, the reconstruction results of the 'T' model are obtained through the FCNN and ResNet reconstruction algorithm. The edge spread function (ESF) is then sampled from the regions of light and dark intersections in the image (The black rectangular regions in the reconstructed images of Figs. 12a and 12b). Next, the derivative of the ESF is computed to obtain the line spread function (LSF). Finally, the LSF is subjected to a fast Fourier transform to obtain the MTF curve for various frequencies, as shown in Figs. 12c and 12d. In imaging, the SR of an imaging system is defined as the reciprocal of the spatial frequency corresponding to an MTF value of 0.1. This study presents the image quality evaluation and SR results in Table 5.
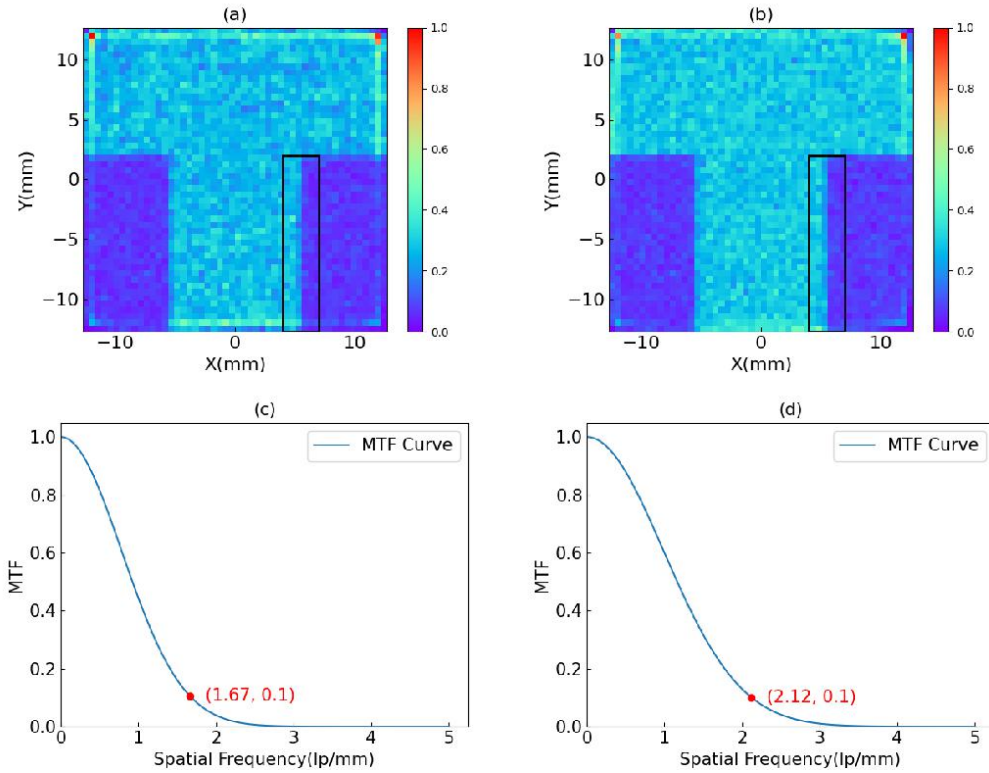

Fig. 12 Calculation results of the SR for neutron imaging: (a) Imaging results of the FCNN's 'T' model; (b) Imaging results of the ResNet's 'T' model; (c) MTF curve of the FCNN's imaging result; (d) MTF curve of the ResNet's imaging result

Table 5 Quality evaluation and SR table for the reconstructed images of the 'T' model using ANN method

	FCNN	ResNet
CNR	219.16	**220.58**

IE	**6.20**	6.09
GM	**0.23**	0.20
SR	0.60	**0.47**

Based on the results in Table 5, both FCNN and ResNet methods can achieve sub-millimeter SR for neutron imaging, with the ResNet method exhibiting an SR of approximately 0.47 mm.

4.2 Gamma imaging

Like neutron imaging, the simulated flood image of the ^{137}Cs point source is shown in Fig. 13. The UFOV and RSD values are obtained from the gamma flood image, as shown in Table 6.
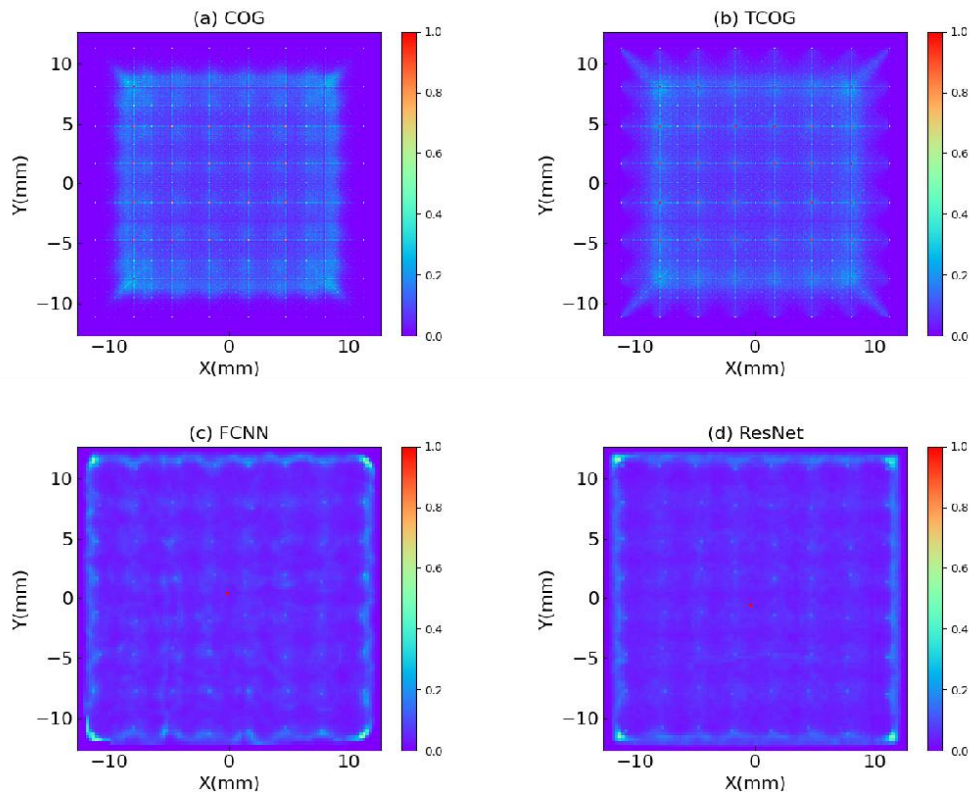

Fig. 13 Simulation results of gamma flood image using different reconstruction algorithms: (a) COG; (b) TCOG; (c) FCNN; (d) ResNet

Table 6 UFOV and RSD values of gamma flood image obtained by various reconstruction algorithms

	COG	TCOG	FCNN	ResNet
UFOV	74.8%	81.1%	93.7%	**94.9%**
RSD	0.874	0.751	0.648	**0.609**

Additionally, further investigations are conducted on the impact of different reconstruction algorithms on gamma imaging. Following the methodology outlined in Section 4.1.4, the material of the 'T' model is modified to tungsten for calculating the

SR of gamma imaging, with the computational results displayed in Fig. 14. Furthermore, the image quality evaluation and SR results are presented in Table 7.
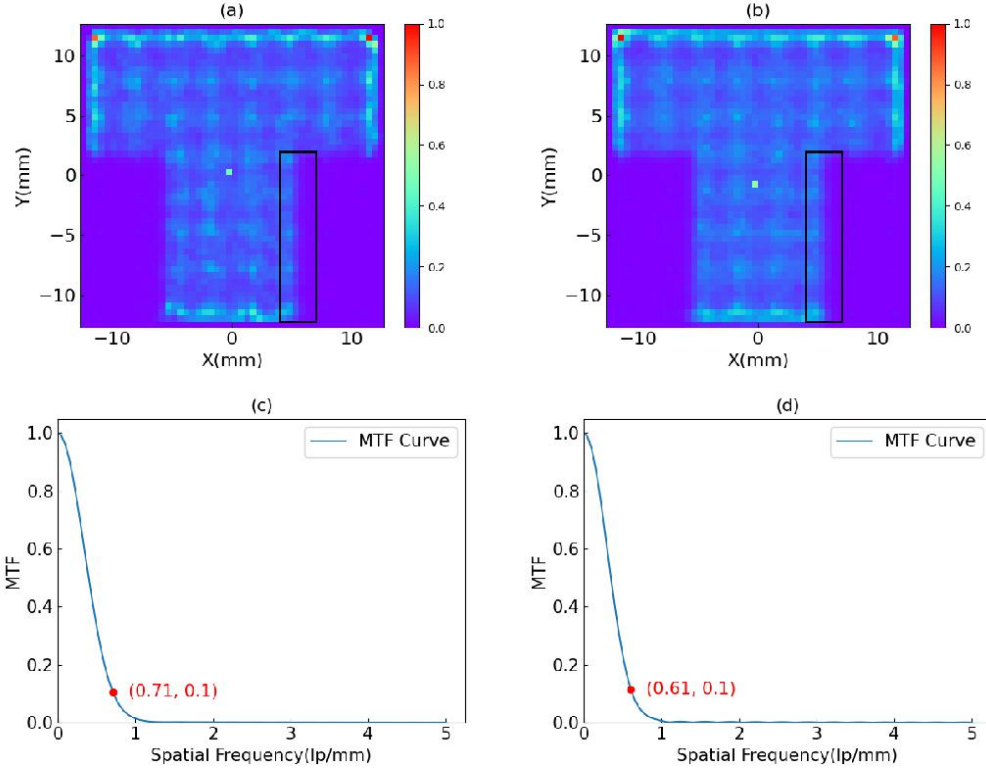

Fig. 14 Calculation results of the SR for gamma imaging: (a) Imaging results of the FCNN's 'T' model; (b) Imaging results of the ResNet's 'T' model; (c) MTF curve of the FCNN's imaging result; (d) MTF curve of the ResNet's imaging result

Table 7 Quality evaluation and SR table for the reconstructed images of the 'T' model using ANN method

	FCNN	ResNet
CNR	227.84	**232.06**
IE	5.10	**5.14**
GM	**0.22**	0.21
SR	**1.41**	1.64

According to the results, it can be observed that the proposed ANN method can achieve better performance on gamma flood image and 'T' model imaging when compared to traditional reconstruction algorithms. The SR of gamma imaging obtained through the ANN method is slightly inferior to that of neutron imaging. To conclude, GS20 can simultaneously achieve neutron and gamma imaging, but the neutron imaging results are superior to gamma imaging. This is because the energy released from neutron reactions is significantly higher than that of gamma-ray, generating more scintillation light, which gives neutron imaging higher contrast and resolution. Additionally, GS20 has low gamma sensitivity, reducing the background noise interference from gamma-ray and improving the signal-to-noise ratio of neutron signals, making neutron imaging clearer.

5. Experimental validation

5.1 Gamma flood image

To evaluate the applicability of the proposed ANN method, the experimentally measured gamma flood image is reconstructed using different reconstruction algorithms. The imaging system is placed in a uniform radiation field generated by an uncollimated ^{137}Cs point source, as shown in Fig. 2 of Section 2. The experimental data of the gamma flood image is obtained and reconstructed using the above algorithms. The reconstruction results are shown in Fig. 15, and the evaluation metric values for UFOV and RSD are summarized in Table 8. Due to the lack of a high-intensity thermal neutron source, the neutron imaging results have not been validated.
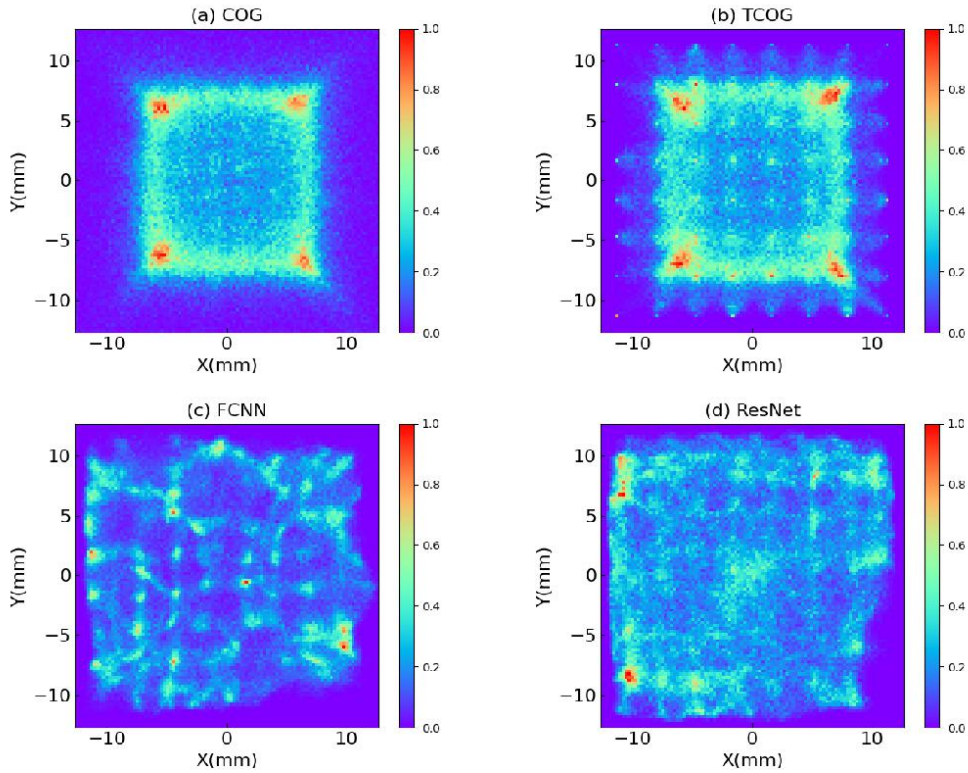

Fig. 15 Experimental results of gamma flood image using different reconstruction algorithms: (a) COG; (b) TCOG; (c) FCNN; (d) ResNet

Table 8 UFOV and RSD values of gamma experimental flood image obtained by various reconstruction algorithms

	COG	TCOG	FCNN	ResNet
UFOV	63.8%	71.7%	85.8%	**90.6%**
RSD	1.010	0.980	0.880	**0.680**

Based on the experimental results, the gamma flood images reconstructed using the COG and TCOG methods demonstrate results similar to the simulation. In contrast, the reconstructed flood images show a reduced reconstruction field of view and poor image uniformity. However, the FCNN and ResNet methods expand the

imaging field of view and improve image uniformity in the experiment, demonstrating the feasibility of the proposed reconstruction algorithms in both simulation and experiment. Additionally, the results indicate that the field of view of the experimentally obtained gamma flood image is smaller than the simulation result, which may be attributed to the combined effects of the following physical mechanisms. First, the actual detection system exhibits significant spatial non-uniformity in light collection efficiency, with substantially higher signal attenuation at the edges compared to the central region, primarily due to the geometric attenuation of photon transmission and interface reflection losses. Second, the mismatch between the temporal characteristics of GS20 luminescence and the time response of SiPM leads to the filtering of some valid signals from edge events. Finally, the non-uniform distribution of lithium-ion concentration in GS20 causes local light yield fluctuations, while the optical crosstalk noise in SiPM further reduces the signal-to-noise ratio. The combined action of these factors results in a smaller reconstructed field of view in the experiment compared to the simulation result.

5.2 Gamma 'T' model imaging experiment

In this study, a 'T' model is constructed using tungsten blocks measuring 5 * 10 * 30 mm³ for gamma imaging, as illustrated in Fig. 16b. This 'T' model is directly placed in front of the GS20. The tungsten blocks block most of the gamma rays emitted by the ^{137}Cs point source, while the SiPM array detects the unblocked rays and records their spatial distribution. Fig. 16a shows a schematic diagram of the 'T' model gamma imaging system. Finally, the imaging results of the 'T' model under different reconstruction algorithms are obtained, as shown in Fig. 17, and the evaluation metric values are summarized in Table 9.
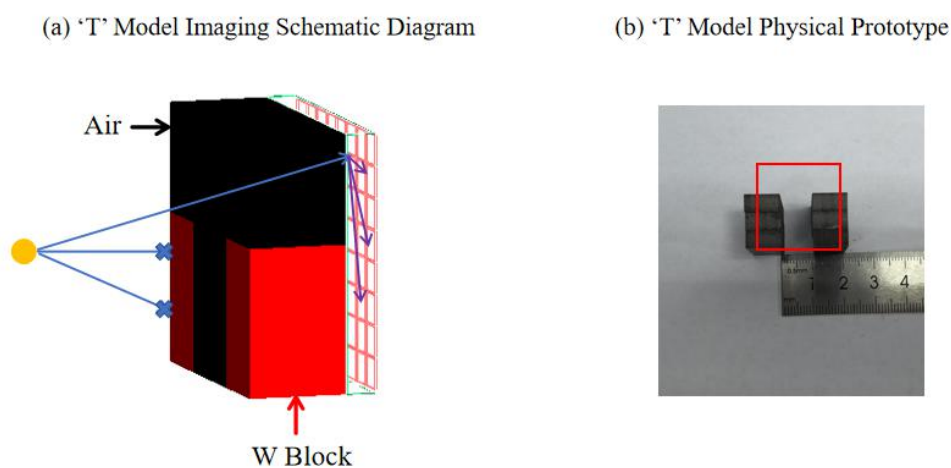

(a) 'T' Model Imaging Schematic Diagram   (b) 'T' Model Physical Prototype

Fig. 16 'T' model imaging system: (a) 'T' model imaging schematic diagram (The optical photon (indicated by purple arrows) is detected by the SiPM array); (b) 'T' model physical prototype (The red rectangle indicates the 'T' model region for imaging)
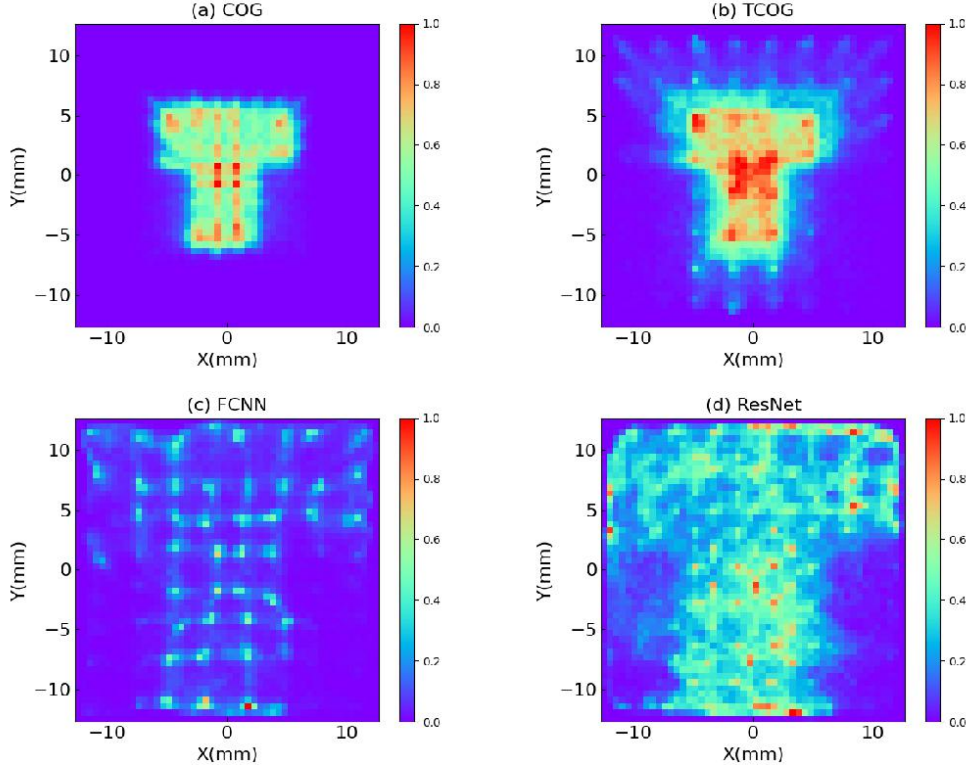
Fig. 17 Imaging experimental results of the gamma 'T' model using different reconstruction algorithms: (a) COG; (b) TCOG; (c) FCNN; (d) ResNet

Table 9 Quality evaluation table for the experimental reconstruction images of the 'T' model using different reconstruction algorithms

	COG	TCOG	FCNN	ResNet
CNR	191.85	**219.57**	209.31	197.79
IE	3.18	5.81	5.47	**7.05**
GM	0.22	0.31	0.32	**0.53**

By analyzing Fig. 17 and Table 9, it is found that although the evaluation metrics of the proposed ANN method are not the best when considering the imaging field of view area together with the three-evaluation metrics CNR, IE, and GM, the ANN method can still achieve better experimental imaging performance compared to traditional reconstruction algorithms. However, it is observed that the imaging results of the ANN method still exhibit some artifacts. This is because the model was trained using simulation data, which will introduce errors when directly applied to experimental data.

6. Conclusion and discussion

In this work, we propose two ANN reconstruction methods and compare them with traditional reconstruction algorithms, including the COG, TCOG, RTP, and PSO-LSE, to estimate the hit position in gamma or neutron imaging systems. The imaging system comprises a monolithic GS20, an 8 * 8 SiPM array, an ESR reflective layer, and a 64-channel ASIC acquisition card. The quality assessment of images is

reconstructed by different algorithms based on the imaging system. Additionally, simulations and experiments are conducted to validate the advantages of the proposed ANN method. The conclusion is summarized as follows:

(1) All reconstruction algorithms can accurately estimate the position of the scintillation event in the central region, while the PSO-LSE and the ANN methods exhibit smaller prediction biases for both the central and edge region, especially the MSE values for the FCNN and ResNet methods are 0.001 and 0.007, respectively, demonstrating superior PNR outcomes compared to traditional reconstruction algorithms.

(2) The COG introduces distortion in the edge region of the flood image, thereby reducing the image UFOV. The PSO-LSE, FCNN, and ResNet methods offer superior reconstruction performance and enhanced image uniformity, achieving a UFOV of 96% and RSD values of less than 1, respectively.

(3) The FCNN method achieves significantly higher CNR, IE, and GM values in neutron imaging, indicating preserved richer image details and more substantial gradient structures. The FCNN method can effectively eliminate the imaging area compression effect at the edges and overcome the predominant limitation of conventional COG (TCOG) methods while sustaining robust noise suppression capabilities.

(4) The knife-edge method calculates the imaging system's SR for the 'T' model. From the MTF curve, the optimal spatial resolutions for neutron and gamma imaging calculated by the ANN method are 0.47 mm and 1.41 mm, respectively.

(5) The UFOV reconstructed by the ANN method in experimental flood images can be improved to approximately 90% while achieving superior imaging performance in comprehensive evaluation metrics compared to traditional reconstruction algorithms.

The ANN method is more adequate for gamma and neutron imaging. However, this study has some limitations. The research only involves gamma and neutron imaging experiments that have not yet been conducted. In the future, experimental data will be collected and combined with simulated data to jointly train the ANN model, enhancing its adaptability to experimental data and thereby further improving experimental imaging quality.

References
1.   Zhan, L., et al., *Development and outlook of advanced nuclear energy technology.* Energy Strategy Reviews, 2021. **34**. https://doi.org/10.1016/j.esr.2021.100630.
2.   Rowlands, J.A., *The physics of computed radiography.* Physics in Medicine and Biology, 2002. **47**(23): p. R123-R166.

https://doi.org/10.1088/0031-9155/47/23/201.

3. Ronowicz-Pilarczyk, J., *RAMAN SPECTROSCOPIC IMAGING - PRACTICAL APPLICATIONS IN INDUSTRIAL PHARMACY AND MEDICAL DIAGNOSTICS: A REVIEW.* Acta Poloniae Pharmaceutica, 2024. **81**(2): p. 215-225. https://doi.org/10.32383/appdr/187033.

4. Steinert, J., M. Salamon, and T. Wittenberg, *Investigation and experimental evaluation of a mono-pixel X-ray system in healthcare.* Current Directions in Biomedical Engineering, 2024. **10**(1): p. 77-80. https://doi.org/10.1515/cdbme-2024-0120.

5. Velayudhan, D., et al., *Autonomous Localization of X-Ray Baggage Threats via Weakly Supervised Learning.* Ieee Transactions on Industrial Informatics, 2024. **20**(4): p. 6563-6572. https://doi.org/10.1109/TII.2023.3348838.

6. Latscha, M., et al., *Performance of X-ray baggage screeners in different work environments: Comparing remote and local cabin baggage screening.* International Journal of Industrial Ergonomics, 2024. **102**. https://doi.org/10.1016/j.ergon.2024.103598.

7. Li, Y.E., et al., *Exploiting activation radiation from neutron tomography reveals the hidden elemental composition of 3D art objects for free.* Scientific Reports, 2024. **14**(1). https://doi.org/10.1038/s41598-024-80047-4.

8. Schillinger, B., et al., *Neutron imaging in cultural heritage research at the FRM ii reactor of the Heinz Maier-Leibnitz center.* Journal of Imaging, 2018. **4**(1): p. 22 (11 pp.)-22 (11 pp.). https://doi.org/10.3390/jimaging4010022.

9. Hoffman, A., et al., *A decade after the Tokyo sarin attack: A review of neurological follow-up of the victims.* Military Medicine, 2007. **172**(6): p. 607-610. https://doi.org/10.7205/MILMED.172.6.607.

10. Phillips, B.J., *How Did 9/11 Affect Terrorism Research? Examining Articles and Authors, 1970-2019.* Terrorism and Political Violence, 2023. **35**(2): p. 409-432. https://doi.org/10.1080/09546553.2021.1935889.

11. Craigie, R.J., et al., *Manchester Arena bombing: lessons learnt from a mass casualty incident.* Bmj Military Health, 2020. **166**(2): p. 72-75. https://doi.org/10.1136/jramc-2018-000930.

12. Wang, B., et al., *Non-destructive testing and evaluation of composite materials/structures: A state-of-the-art review.* Advances in Mechanical Engineering, 2020. **12**(4). https://doi.org/10.1177/1687814020913761.

13. Anger, H.O., *SCINTILLATION CAMERA.* Review of Scientific Instruments, 1958. **29**(1): p. 27-33. https://doi.org/10.1063/1.1715998.

14. Zhang, C.Q., et al., *Experimental Demonstration of a Tunable Energy-Selective Gamma-Ray Imaging System Based on Recoil Electrons.* Sensors, 2024. **24**(12). https://doi.org/10.3390/s24123736.

15. Karafasoulis, K., et al., *A machine learning approach in the estimation of a radioactive source position using a coded aperture device.* Journal of Instrumentation, 2023: p. C01062 (11 pp.)-C01062 (11 pp.). https://doi.org/10.1088/1748-0221/18/01/C01062.

16. Wu, Y.C., et al., *Virtual source approach for maximizing resolution in*

high-penetration gamma-ray imaging. Matter and Radiation at Extremes, 2024. **9**(3). https://doi.org/10.1063/5.0179781.

17. Sarkar, P.S., *Safety, Regulations, Metrology and Standards in Neutron Imaging*, in *Neutron Imaging: Basics, Techniques and Applications*, D.K. Aswal, P.S. Sarkar, and Y.S. Kashyap, Editors. 2022, Springer Singapore: Singapore. p. 207-235. https://doi.org/10.1007/978-981-16-6273-7.

18. Craft, A.E., et al. *Conversion from film to image plates for transfer method neutron radiography of nuclear fuel.* in *8th International Topical Meeting on Neutron Radiography (ITMNR)*. 2016. Peking Univ, Beijing, PEOPLES R CHINA. https://doi.org/10.1016/j.phpro.2017.06.010.

19. Raghu, N., et al. *Neutron radiographic inspection of industrial components using Kamini neutron source facility.* in *International Conference on Neutron and X-Ray Scattering 2007*. 2007. Serpong, INDONESIA. https://doi.org/10.1063/1.2906066.

20. Owejan, J.P., et al., *Direct measurement of lithium transport in graphite electrodes using neutrons.* Electrochimica Acta, 2012. **66**: p. 94-99. https://doi.org/10.1016/j.electacta.2012.01.047.

21. Kino, K., et al. *First Imaging Experiment of a Lithium Ion Battery by a Pulsed Neutron Beam at J-PARC/MLF/BL09.* in *10th World Conference on Neutron Radiography (WCNR)*. 2014. Grindelwald, SWITZERLAND. https://doi.org/10.1016/j.phpro.2015.07.087.

22. Sun, F., et al., *Complementary X-ray and neutron radiography study of the initial lithiation process in lithium-ion batteries containing silicon electrodes.* Applied Surface Science, 2017. **399**: p. 359-366. https://doi.org/10.1016/j.apsusc.2016.12.093.

23. Fabbri, A., et al., *A new iterative algorithm for pixilated and continuous scintillating crystal.* Nuclear Instruments & Methods in Physics Research Section a-Accelerators Spectrometers Detectors and Associated Equipment, 2011. **648**: p. S79-S84. https://doi.org/10.1016/j.nima.2010.12.136.

24. Lerche, C.W., et al., *Maximum likelihood positioning for gamma-ray imaging detectors with depth of interaction measurement.* Nuclear Instruments & Methods in Physics Research Section a-Accelerators Spectrometers Detectors and Associated Equipment, 2009. **604**(1-2): p. 359-362. https://doi.org/10.1016/j.nima.2009.01.060.

25. Pani, R., et al., *Position algorithm for monolithic scintillation crystals based on charge projection readout.* Journal of Instrumentation, 2016. **11**. https://doi.org/10.1088/1748-0221/11/01/C01061.

26. Shi, R.G., Y. Chen, and M.F. Wei, *Least squares estimate algorithm based on particle swarm optimization for position reconstruction of scintillation crystal.* Journal of Instrumentation, 2018. **13**. https://doi.org/10.1088/1748-0221/13/12/P12029.

27. Fabbri, A., et al., *Study of position reconstruction of a LaBr3: Ce continuous scintillation crystal for medical applications.* Journal of Instrumentation, 2013. **8**. https://doi.org/10.1088/1748-0221/8/12/P12010.

28. Jeong, M.H., et al. *Position mapping, energy calibration, and flood correction improve the performances of small gamma camera using PSPMT*. in *IEEE Nuclear Science Symposium/Medical Imaging Conference*. 2003. Portland, OR. https://doi.org/10.1109/NSSMIC.2003.1352295.

29. Chung, Y.H., et al., *Evaluation of maximum-likelihood position estimation with Poisson and Gaussian noise models in a small gamma camera*. Ieee Transactions on Nuclear Science, 2004. **51**(1): p. 101-104. https://doi.org/10.1109/TNS.2003.823053.

30. Shi, R.G., et al., *Experimental evaluation of reconstruction algorithms for scintillation crystal array based on charge projection readout*. Nuclear Instruments & Methods in Physics Research Section a-Accelerators Spectrometers Detectors and Associated Equipment, 2019. **937**: p. 117-124. https://doi.org/10.1016/j.nima.2019.05.064.

31. Correia, P.M.M., et al., *Precise positioning of gamma ray interactions in multiplexed pixelated scintillators using artificial neural networks*. Biomedical Physics & Engineering Express, 2024. **10**(4). https://doi.org/10.1088/2057-1976/ad4f73.

32. Morozov, A., et al., *SiPM-based neutron Anger camera with auto-calibration capabilities*. Journal of Instrumentation, 2019. **14**. https://doi.org/10.1088/1748-0221/14/03/P03016.

33. Wang, P.H., et al., *Optical simulation of the non-uniformity for the LYSO crystal of the HERD calorimeter*. Nuclear Instruments & Methods in Physics Research Section a-Accelerators Spectrometers Detectors and Associated Equipment, 2024. **1062**. https://doi.org/10.1016/j.nima.2024.169209.

34. Agostinelli, S., et al., *GEANT4-a simulation toolkit*. Nuclear Instruments & Methods in Physics Research Section a-Accelerators Spectrometers Detectors and Associated Equipment, 2003. **506**(3): p. 250-303. https://doi.org/10.1016/S0168-9002(03)01368-8.

35. Song, R.-Q., et al., *A high light yield neutron scintillator based on Ce3+-doped lithium glass*. Chinese Physics B, 2025. https://doi.org/10.1088/1674-1056/adb94b.

36. Sui, Z., et al., *Glass scintillator: A window to future high-energy radiation detection*. The Innovation, 2025: p. 100878. https://doi.org/10.1016/j.xinn.2025.100878.

37. Scrimger, J.W. and R.G. Baker, *INVESTIGATION OF LIGHT DISTRIBUTION FROM SCINTILLATIONS IN A GAMMA CAMERA CRYSTAL*. Physics in Medicine and Biology, 1967. **12**(1): p. 101-&. https://doi.org/10.1088/0031-9155/12/1/411.

38. Han, J.F., et al., *Pulse characteristics of CLYC and piled-up neutron-gamma discrimination using a convolutional neural network*. Nuclear Instruments & Methods in Physics Research Section a-Accelerators Spectrometers Detectors and Associated Equipment, 2022. **1028**. https://doi.org/10.1016/j.nima.2022.166328.

39. Yi, C.Q., et al., *Discrimination of piled-up neutron-gamma pulses using*

charge comparison method and neural network for CLYC detectors. Nuclear Instruments & Methods in Physics Research Section a-Accelerators Spectrometers Detectors and Associated Equipment, 2023. **1055**. https://doi.org/10.1016/j.nima.2023.168561.

40.   Xu, Z.X., et al., *Lower-Weight Landmine Detection Under Various Buried Conditions Based on PGNAA and Machine Learning.* Nuclear Technology, 2022. **208**(12): p. 1847-1857. https://doi.org/10.1080/00295450.2022.2076489.

41.   Hsu, K.Y., H.Y. Li, and D. Psaltis, *HOLOGRAPHIC IMPLEMENTATION OF A FULLY CONNECTED NEURAL NETWORK.* Proceedings of the Ieee, 1990. **78**(10): p. 1637-1645. https://doi.org/10.1109/5.58357.

42.   He, K.M., et al. *Deep Residual Learning for Image Recognition.* in *2016 IEEE Conference on Computer Vision and Pattern Recognition (CVPR).* 2016. Seattle, WA. https://doi.org/10.1109/CVPR.2016.90.

43.   Lee, S. and Y. Lee, *Performance evaluation of median-modified Wiener filter algorithm in high-resolution complementary metal-oxide-semiconductor radio-magnetic X-ray imaging system: An experimental study.* Nuclear Instruments & Methods in Physics Research Section a-Accelerators Spectrometers Detectors and Associated Equipment, 2021. **1010**. https://doi.org/10.1016/j.nima.2021.165509.

44.   Zhang, Y.R., et al., *Design and performance of a cone-beam computed tomography system for small animals.* Nuclear Instruments & Methods in Physics Research Section a-Accelerators Spectrometers Detectors and Associated Equipment, 2023. **1048**. https://doi.org/10.1016/j.nima.2022.168003.

45.   Hang, J., et al., *Ring artifact suppression and removal algorithm for an X-ray cone beam CT system.* Nuclear Instruments and Methods in Physics Research Section A: Accelerators, Spectrometers, Detectors and Associated Equipment, 2025. **1072**: p. 170217. https://doi.org/10.1016/j.nima.2025.170217.

46.   Shannon, C.E., *A MATHEMATICAL THEORY OF COMMUNICATION.* Bell System Technical Journal, 1948. **27**(3): p. 379-423. https://doi.org/10.1002/j.1538-7305.1948.tb01338.x.

47.   Brown, L.G., *A SURVEY OF IMAGE REGISTRATION TECHNIQUES.* Computing Surveys, 1992. **24**(4): p. 325-376. https://doi.org/10.1145/146370.146374.

48.   Donoho, D.L. and I.M. Johnstone, *IDEAL SPATIAL ADAPTATION BY WAVELET SHRINKAGE.* Biometrika, 1994. **81**(3): p. 425-455. https://doi.org/10.1093/biomet/81.3.425.

49.   Starck, J.L., et al., *Gray and color image contrast enhancement by the curvelet transform.* Ieee Transactions on Image Processing, 2003. **12**(6): p. 706-717. https://doi.org/10.1109/TIP.2003.813140.

50.   Boreman, G.D., *Modulation transfer function in optical and electro-optical systems.* Vol. 4. 2001: SPIE press Bellingham, Washington. https://doi.org/10.1117/3.419857.